ACS Catalysis
Research Article
pubs.acs.org/acscatalysis

Effect of Oxygen Defects on the Catalytic Performance of VO_x/CeO_2 Catalysts for Oxidative Dehydrogenation of Methanol

Yan Li,[†] Zhehao Wei,[†] Feng Gao,*[‡] Libor Kovarik,[‡] Rebecca A. L. Baylon,[†] Charles H. F. Peden,[‡] and Yong Wang*[†,‡]

[†]Gene and Linda Voiland School of Chemical Engineering and Bioengineering, Washington State University, Pullman, Washington 99164, United States

[‡]Institute for Integrated Catalysis, Pacific Northwest National laboratory, Richland, Washington 99354, United States

Supporting Information

ABSTRACT: In this work, CeO_2 nanocubes with controlled particle size and dominating (100) facets are synthesized as supports for VO_x catalysts. Combined TEM, SEM, XRD, and Raman study reveals that the oxygen vacancy density of CeO_2 supports can be tuned by tailoring the particle sizes without altering the dominating facets, where smaller particle sizes result in larger oxygen vacancy densities. At the same vanadium coverage, the VO_x catalysts supported on small-sized CeO_2 supports with higher oxygen defect densities exhibit promoted redox property and lower activation energy for methoxyl group decomposition, as evidenced by H_2-TPR and methanol TPD study. These results further confirm that the presence of oxygen vacancies plays an important role in promoting the activity of VO_x species in methanol oxidation.

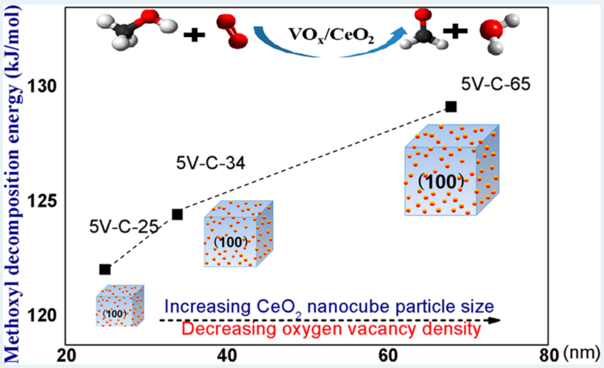

KEYWORDS: *ceria nanocubes, (100), VO_x catalysts, methanol, ODH*

1. INTRODUCTION

Supported vanadia catalysts have received much attention because of their good activity and selectivity in a number of selective oxidation reactions.[1−3] The underlying supports have shown strong effect on the activity of supported vanadium oxide catalysts in oxidation reactions.[4−6] For instance, the turnover frequency (TOF) for monolayer VO_x catalysts supported on various supports in oxidative dehydration (ODH) of methanol follows the order of $VO_x/CeO_2 > VO_x/ZrO_2 > VO_x/TiO_2 \gg VO_x/Al_2O_3 \gg VO_x/SiO_2$.[5,7] However, despite of the extensive efforts, the origin of the support effect is still under debate. Wachs and co-workers proposed that the support effect is related to the Sanderson cation electronegativity of the underlying supports: more electropositive support cations in supported VO_x catalysts lead to a higher TOF in the ODH of methanol.[7] Bell and co-workers correlated the TOF of supported VO_x catalysts for methanol oxidation with the oxygen vacancy formation energy of the supports. Experimental observation on CeO_2-, ZrO_2-, TiO_2-, Al_2O_3-, and SiO_2-supported VO_x shows that with lower oxygen vacancy formation energy on the supports such as CeO_2 and TiO_2, a higher TOF for methanol oxidation is observed.[8] Similarly, Schomäcker and co-workers investigated the influence of support on the catalytic performance of vanadia catalysts in the ODH of ethanol and propane. They found that vanadia catalysts with lower oxygen defect formation enthalpies such as VO_x/TiO_2, VO_x/CeO_2, and VO_x/ZrO_2 exhibit lower apparent activation energy for ethanol and propane oxidation.[9] It is worth noting that for supported vanadate catalysts, the degree of oligomerization for surface vanadate species varies as a function of the precursor used during synthesis and total V coverages.[5,10] For two electron reactions that involve transferring of one O atom, such as methanol ODH, the relative activities for isolated and oligomeric surface VO_4 species are essentially identical, since only one surface VO_4 unit is required for such reactions.[11]

Recent success in the synthesis of CeO_2 nanoparticles with varying exposed facets allows us to further explore the effect of oxide support on the catalytic activity of VO_x catalysts in selective oxidation reactions. In our recent research, vanadia model catalysts supported on well-defined ceria nanocubes, nanorods, and nanopolyhedras with dominating low index facets, that is, (100) for ceria nanocubes, (110) and (100) for ceria nanorods, (111) for ceria nanopolyhedras, were prepared and studied in methanol oxidation. We found a clear correlation between the catalytic activity of VO_x active sites and oxygen vacancy density of the supports.[12] Similarly, recent research conducted by Wu et al. on VO_x/CeO_2 rod and octahedra shows

Received: December 24, 2014
Revised: April 5, 2015
Published: April 6, 2015

DOI: 10.1021/cs502084g
ACS Catal. 2015, 5, 3006−3012

that the VO_x/CeO_2 nanorods with both (110) and (100) facets possess more oxygen vacancies and exhibit lower apparent activation energies for selective oxidation of iso-butane.[13] However, variations in the size of well-defined ceria nanoparticles and their correlation with oxygen vacancies and, subsequently, their effects on the catalytic properties of supported VO_x catalysts have not been systematically studied, mainly obscured by some unknown intrinsic differences in the nature of the various supports and surface structure differences for different facets of the same support material (i.e., CeO_2).

To better examine the role of well-defined ceria nanoparticle size and associated oxygen defects for the oxidative dehydrogenation reaction on supported vanadia catalysts, we prepared a series of ceria nanocubes with a single dominant low index facet (i.e., (100)) but with different particle sizes to minimize effects from differences in the nature of metal oxide supports and the presence of mixed facets. The surface structure and redox property of these well-defined VO_x/CeO_2 model catalysts were investigated using various techniques, and their catalytic performance was examined using methanol oxidation as a probe reaction.

2. EXPERIMENTAL METHOD

2.1. Size-Controlled Synthesis of CeO_2 Nanocubes. CeO_2 nanocubes with varying particle sizes were prepared via a hydrothermal method using $Ce(NO_3)_3 \cdot 6H_2O$ as the ceria source and NaOH as precipitator.[14] The sizes of the CeO_2 nanocubes were controlled by varying the NaOH concentration. Specifically, the desired amount of $Ce(NO_3)_3 \cdot 6H_2O$ (Sigma-Aldrich, 99.999%) and NaOH were dissolved in DI water, respectively. The obtained $Ce(NO_3)_2$ aqueous solution was then added to NaOH aqueous solution dropwise under vigorous stirring and kept for 30 min. The obtained purple solution was then transferred to an autoclave and subjected to hydrothermal treatment under various conditions. The obtained white suspension was centrifuged, and the precipitated CeO_2 paste was then thoroughly washed with DI water and ethanol several times to remove sodium and other impurities.[15] The detailed hydrothermal preparation conditions and physical properties of CeO_2 nanocubes are listed in Table 1. The prepared CeO_2 nanocubes were denoted as CeO_2−C-68, CeO_2−C-34 and CeO_2−C-25 respectively, where the numbers represent the average size of the corresponding CeO_2 nanocube supports based on TEM and SEM observation.

Table 1. Hydrothermal Synthesis Conditions and Physical Properties of CeO_2−C Supports

support	C_{Ce} (mol/L)	C_{NaOH} (mol/L)	temp (°C)	time (h)	SSA (m^2/g)
CeO_2−C-25	0.05	6	180	24	27.2
CeO_2−C-34	0.05	12	180	24	14.0
CeO_2−C-68	0.05	9	180	24	10.4

2.2. VO_x/CeO_2 Catalyst Preparation. VO_x catalysts supported on CeO_2 nanocubes were prepared by an incipient wetness impregnation method. The obtained CeO_2 nanocube supports were first calcined at 400 °C for 4 h prior to use. These supports were then impregnated with an aqueous ammonium metavanadate solution prepared by dissolving desired amounts of ammonium metavanadate (NH_4VO_3, Sigma-Aldrich, 99.999%) in an aqueous solution of oxalic acid ($H_2C_2O_4$, Sigma-Aldrich, 99.999%) with a $NH_4VO_3/H_2C_2O_4$ molar ratio of 1/2. The samples were dried at ambient temperature for 12 h and calcined at 400 °C for 4 h in air. The vanadia loadings on the three catalysts were fixed at 5 V/nm^2, which is ~1 monolayer coverage, according to literature reports by others and us.[12,16] The vanadia catalysts supported on different CeO_2 nanocube supports are denoted as 5 V−C-68, 5 V−C-34, and 5 V−C-25, respectively. Detailed vanadia loading and V density for the three catalysts are shown in Table 2.

Table 2. Vanadia Loading and Densities in VO_x/CeO_2−C Catalysts

catalysts	V_2O_5 loading (wt %)	V density (V atoms/nm^2)
5 V−C-25	1.99	5
5 V−C-34	1.05	5
5 V−C-68	0.78	5

2.2. Catalyst Characterization. TEM analysis was performed with an aberration-corrected FEI Titan 80-300 operated at 300 keV. SEM images were acquired using an FEI Helios 600 NanoLab FIB-SEM (focused ion beam-scanning electron microscope). The specific surface areas (SSA) of the samples were measured using N_2 adsorption−desorption isotherms recorded at −196 °C on a QuantaChrome Autosorb-6 automatic physisorption analyzer. The samples were degassed under vacuum at 180 °C for 4 h prior to measurements. The Brunauer−Emmett−Teller (BET) method was used to calculate the SSAs. H_2 temperature-programmed reduction (TPR) was performed on a Micromeritics AutoChem II 2920 chemisorption analyzer equipped with a thermal conductivity detector. The samples were first pretreated with 5% O_2/He at 400 °C for 30 min, and then the sample temperature was ramped from ambient to 900 °C in 5% H_2/Ar at 10 °C/min. X-ray diffraction (XRD) measurement was carried out with a Philips PW3040/00 X'Pert MPD system equipped with a Cu source ($\lambda = 1.5406$ A). Raman spectra were acquired using a Horiba LabRAM HR Raman/FTIR microscope equipped with a 532 nm (Ventus LP 532) laser source and a Synapse charge coupled device detector. Samples were dehydrated in an in situ sample cell (Linkam CCR1000) at 400 °C (ramp rate 10 °C/min) under 10% O_2/He (30 mL/min) for 30 min. After cooling to ambient temperature, Raman spectra of the dehydrated samples were recorded.

CH_3OH-TPD experiments were conducted using the AutoChem II 2920 Chemisorption Analyzer coupled with an online mass spectrometer (MS, Quadra 220). The sample was pretreated with 10% O_2/He at 400 °C for 30 min. After cooling to 100 °C and being flushed in He for 40 min, the sample was exposed to repeated 0.5 mL 6% CH_3OH/He pulses until saturation. The sample was purged at 100 °C with He for 1 h to remove physically adsorbed methanol, and then the temperature was brought up to 500 °C at a ramping rate of 10 °C/min. The online MS was used to record desorbed species as a function of temperature.

3. RESULTS

3.1. Structure Analysis of CeO_2 Nanocubes. TEM or SEM images of the three calcined CeO_2 nanocube samples are shown in Figure 1. As is shown in Figure 1 a−c, all CeO_2 particles exhibit a cubic shape, and the nanocube morphology is well maintained after calcination. High-resolution TEM images were obtained with the incident electron beam perpendicular to the sampling facet, and Figure 1d shows a representative image.

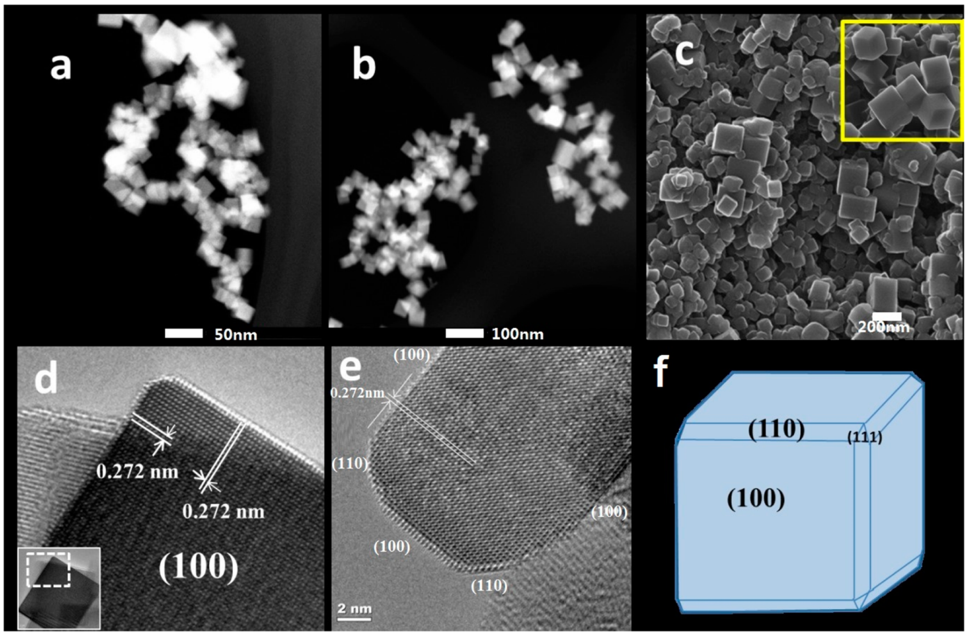

Figure 1. TEM (a, b, d, and e) or SEM images (c) of CeO_2 nanocubes (a, CeO_2−C-25; b, CeO_2−C-34; c, CeO_2−C-68; d and e, HR-TEM image of CeO_2 nanocubes (d, CeO_2−C-34; e, CeO_2−C-25); f, schematic structure of CeO_2 nanocubes).

The interplanar distance of the clearly resolved 2D lattice fringes is 0.272 nm, which corresponds to the {200} lattice spacing of the FCC (face centered cubic) structure. The {200} lattice fringes are either parallel or perpendicular to the edges of the CeO_2 nanocubes, indicating that the CeO_2 nanocubes are enclosed by six (100) facets. HR-TEM image in Figure 1e shows the presence of a small portion of (110) planes at the edges of CeO_2 nanocubes. The presence of a negligible amount of (111) facets has also been reported in cubic CeO_2.[17] It is worth noting that the contribution from (110) and (111) facets to the total surface area is very minor, estimated to be <9% from TEM for all of the CeO_2 nanocubes samples used in this study (Figure S1).

The size distribution histograms of the prepared CeO_2 nanocube samples are shown in Figure 2. The majority of the particles in CeO_2−C-25 display sizes between ∼15−33 nm. For the CeO_2−C-34 sample, the particles are mainly between 24 and 43 nm. The CeO_2−C-68 samples show a wide size distribution between 50 and 200 nm, with the majority of the particles ranging from 45 to 72 nm. These results are fully consistent with BET analysis (Table. 1), with smaller-sized CeO_2 nanocubes displaying larger specific surface areas.

3.2. XRD. Figure 3 shows the XRD patterns of the CeO_2 nanocubes and the 5 V-CeO_2−C catalysts. All three of the CeO_2 supports exhibit a pure fluorite cubic structure (space group *Fm*3*m* (225)) with diffraction peaks at 28.5, 33.1, 47.4, 56.3, 59.1, 69.4, 76.8, and 79.4°, which can be attributed to the (111), (200), (220), (311), (222), (400), (331), and (420) facets of CeO_2, according to JCPDS 34-0394. The average particle sizes for the CeO_2 nanocubes, which are 28 nm for CeO_2−C-25, 35 nm for CeO_2−C-34, and 61 nm for CeO_2−C-68, respectively, were estimated using the Scherrer equation. These estimations are in very good agreement with the TEM and SEM results. XRD patterns for the 5 V-CeO_2−C samples exhibit only the characteristic peaks for CeO_2, and no diffraction features from crystalline vanadia species (i.e., V_2O_5 with diffraction peaks at 2θ = 20.39°, 26.21°, 31.09°, 34.41°) are observed.[18] This indicates that the vanadia species are finely dispersed on the surface of CeO_2 nanocubes. It has been reported that surface vanadia species can react with CeO_2 to form $CeVO_4$ when calcined at high temperatures.[19] No diffraction peaks for $CeVO_4$ ($2\ \theta$ = 24.0° and 32.5°) were observed.

3.3. H_2-TPR. H_2-TPR was used to investigate the redox properties of the CeO_2 nanocube supports and the VO_x/CeO_2 catalysts, and the results are shown in Figure 4. For the CeO_2 nanocube supports, the reduction features between ∼280−650 °C are attributed to Ce^{4+}/Ce^{3+} reduction of surface CeO_2, and the peaks between ∼650−860 °C correspond to the reduction of bulk CeO_2 oxide.[20] As shown in Figure 4, each support appears to have two surface reduction peaks, and the lower-temperature one is considerably weaker. Interestingly, the reduction temperatures of surface CeO_2 increase with increasing particle size (i.e., 352/468 °C for CeO_2−C-25, 405/557 °C for CeO_2−C-34, and 415/578 °C for CeO_2−C-68). For the 5 V-CeO_2−C catalysts, features between ∼450 and 660 °C are due mainly to the reduction of VO_x species. It is worth noting that two reduction peaks, one centered at ∼540 °C and the other at ∼580 °C, are clearly observed in this region. The lower reduction peaks centered around 540 °C are tentatively assigned to reduction of VO_x species supported on smaller CeO_2 particles, and at the ones at 583 °C are assigned to a reduction of surface VO_x species supported on larger CeO_2 particles. These assignments correlate well with the particle size distribution displayed in Figure 2.

3.4. Raman Spectra. The surface structures of the CeO_2 supports and the VO_x/CeO_2 catalysts were investigated using Raman spectroscopy. Raman spectroscopy is a powerful tool to probe oxygen vacancies in ceria. The relative intensity ratio of the defect band (I_D) and the F_{2g} band ($I_{F_{2g}}$) of the CeO_2 fluorite phase (i.e., $I_D/I_{F_{2g}}$) can be used as an indicator of the oxygen defects density. Successful cases can be found in recent publications by others.[21,22] Figure 5 shows Raman spectra of the CeO_2 nanocubes. The band at 462 cm^{-1} corresponds to the F_{2g} mode of CeO_2 supports and the two much weaker bands at

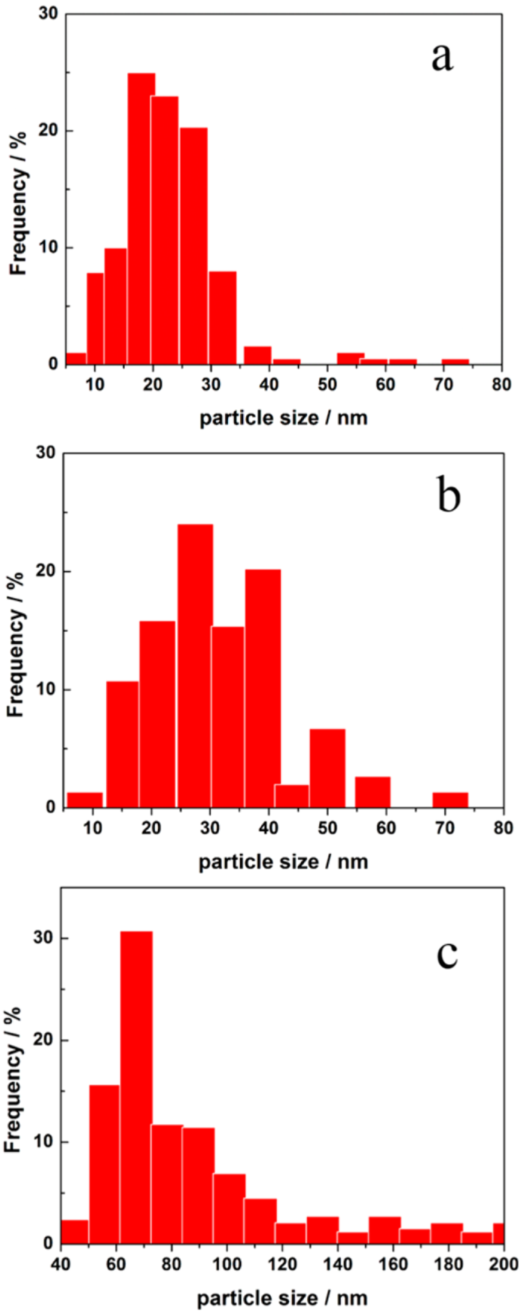

Figure 2. Particle size distribution of CeO_2 nanocube supports (a, CeO_2-C-25; b, CeO_2-C-34; c, CeO_2-C-68).

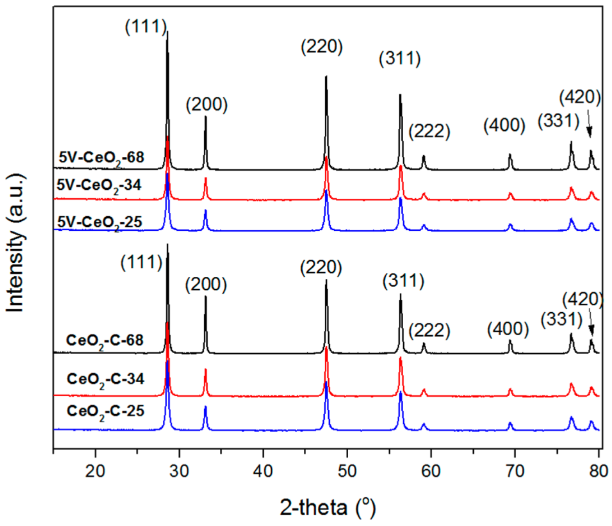

Figure 3. XRD patterns of CeO_2-C supports and 5 V-CeO_2-C catalysts.

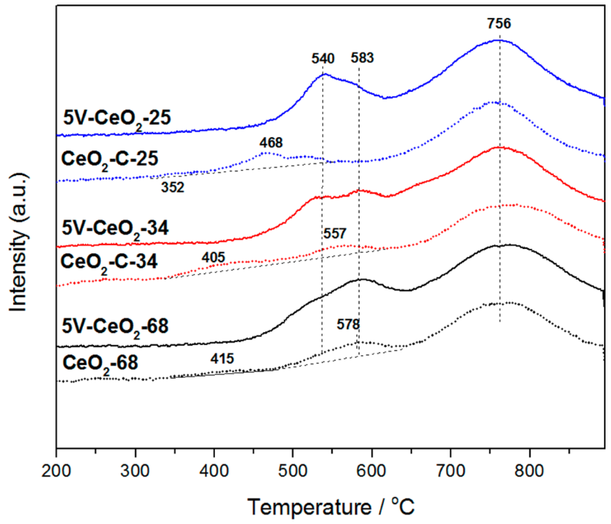

Figure 4. H_2-TPR profiles of the CeO_2 supports and 5 V-CeO_2-C catalysts.

249 and 594 cm^{-1} can be assigned to the second-order transverse acoustic (2TA) mode of CeO_2 and the oxygen defect-induced (D) mode of CeO_2 supports.[22] All the Raman spectra were normalized to the same height of the band at 462 cm^{-1} for the purpose of directly comparing defect densities. As shown in Figure 5, the oxygen vacancy density on three CeO_2 nanocubes follows the order of $CeO_2-C-25 > CeO_2-C-34 > CeO_2-C-68$.

Raman spectra of the V═O stretching vibrational region for the 5 V-CeO_2-C samples are displayed in Figure 6. Two V═O vibration bands at ~1018 and 1037 cm^{-1} are observed for each sample, which is consistent with our previous Raman results on VO_x/CeO_2-C catalyst with the same surface vanadia coverage of 5 V atoms/nm^2.[12] On the basis of previous studies on VO_x/CeO_2 by Baron et al. and Wu et al, the former is attributed to VO_x dimers, and the latter, to VO_x trimers.[23,24] In agreement with the XRD results, no band corresponding to crystalline V_2O_5 (994 cm^{-1}) is observed.[19] These results indicate that at one monolayer coverage, the highly dispersed surface VO_x species are present as two-dimensional dimers and trimers on the (100) facets of CeO_2 nanocubes. Figure 7 shows Raman spectra of the low-frequency region for the 5 V-CeO_2 catalysts. With vanadia deposition, the densities of oxygen vacancy still follow the same trend as the CeO_2 supports, that is, 5 V−C-25 > 5 V−C-34 > 5 V−C-68. This has important implications suggesting some oxygen vacancies in CeO_2 are subsurface in nature and, therefore, are not removable by surface VO_x species. This will be addressed in more detail in the Discussion section.

3.5. Methanol TPD. To explore the effect of oxygen defects on the activity of VO_x/CeO_2 in methanol oxidation, CH_3OH-TPD was used to probe the methoxyl group decomposition on the surfaces of the catalysts. Masses corresponding to desorbed methanol, HCHO, H_2O, CO, and CO_2 were simultaneously

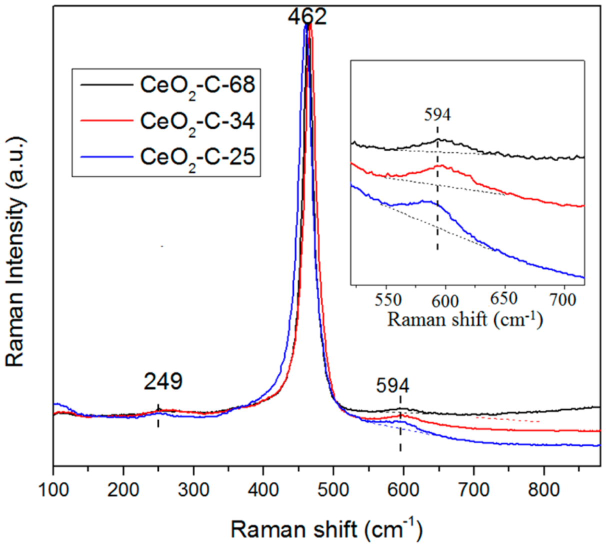

Figure 5. Raman spectra of CeO_2−C supports.

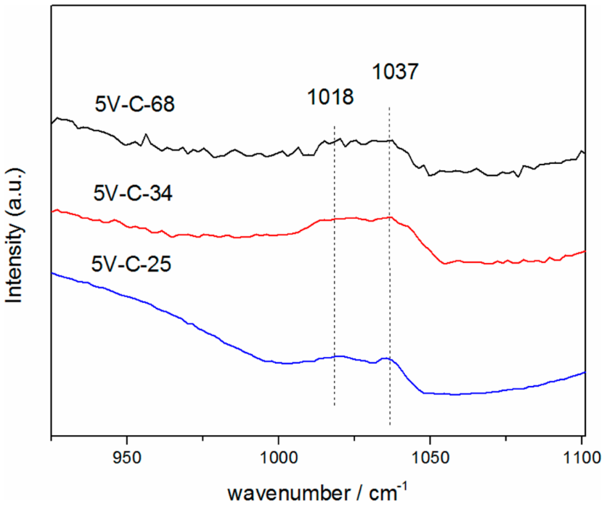

Figure 6. Raman spectra of 5 V-CeO_2−C catalysts (V═O stretching region).

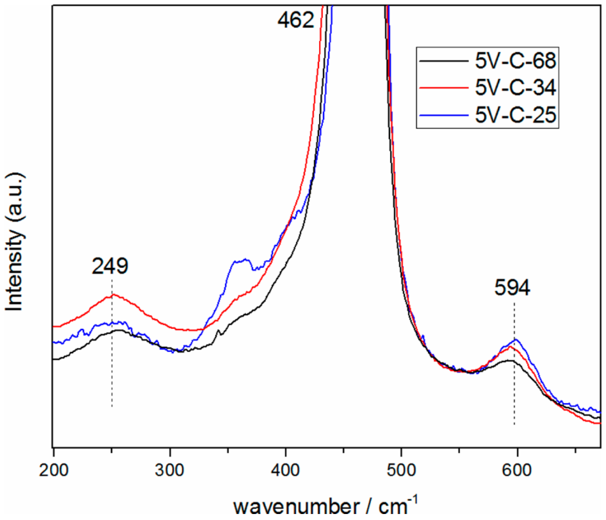

Figure 7. Raman spectra of 5 V-CeO_2−C catalysts (low-frequency region).

monitored during the TPD experiments. HCHO (m/z = 30) desorption curves are shown in Figure 8. Other products are shown only in the Supporting Information (Figure S2) for brevity because they did not provide compelling information. Note that in methanol TPD on supported VO_x catalysts, it is possible to observe two HCHO deposition states, that is, lower-temperature desorption from fully oxidized VO_x sites and higher-temperature desorption from reduced VO_x sites as discovered by Vohs and co-workers.[25] In the present study, only one symmetric CH_2O desorption peak is observed on our VO_x/CeO_2 samples with monolayer VO_x coverage, indicating that HCHO formation proceeds only on fully oxidized vanadia sites. This result is also supported by a recent theoretical and experimental study by Freund and co-workers[26] on VO_x/CeO_2 (111) thin films, which has shown that, with the presence of oxygen defects, V maintains a 5+ oxidation state, whereas Ce^{4+} is partially reduced to Ce^{3+} with additional electrons occupying a localized Ce 4f state. In this case, a second HCHO desorption peak from reduced V sites is not expected, as confirmed from our results.

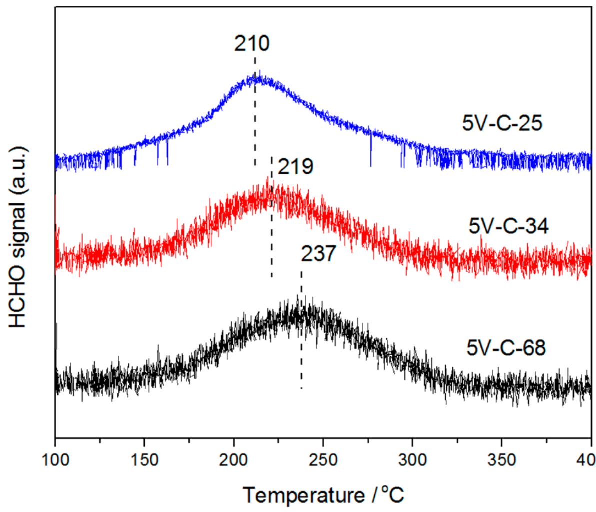

Figure 8. CH_2O signal in methanol-TPD for VO_x/CeO_2−C catalysts (m/z = 30).

With increasing particle sizes of the CeO_2 supports, HCHO desorption progressively shifts to higher temperatures, with peak temperatures at 210 °C for 5 V−C-25, 219 °C for 5 V−C-34, and 237 °C for 5 V−C-68. The decomposition of the surface methoxyl groups on supported VO_x catalysts has been reported to occur on surface vanadia redox sites and follow a first-order reaction.[27] Compared with methanol TPD results by Feng and Vohs[25] conducted at high-vacuum conditions under which methanol readsorption is not expected, the HCHO desorption peak widths in the present study are not broadened, indicating that our TPD results are not significantly affected by readsorption and diffusion for high-surface-area samples; therefore, the activation energy (E_a) for HCHO formation from surface CH_3O− intermediates decomposition on our VO_x/CeO_2−C catalysts can be estimated via the Redhead equation $(E_a/(RT_p^2)) = (\gamma/\beta)\ \exp(-(E_a/(RT_p)))$, where T_p represents the TPD peak maximum; β is the heating rate, which is 10 °C/min in this case; and R is the gas constant.[25] Assuming a pre-exponential factor of ∼10^{13} s^{-1},[27] the calculated activation energies for methoxy decomposition on 5 V−C-25, 5 V−C-34, and 5 V−C-68 are 122.1, 124.5, and 129.2 kJ/mol, respectively. These results are shown in Figure 9.

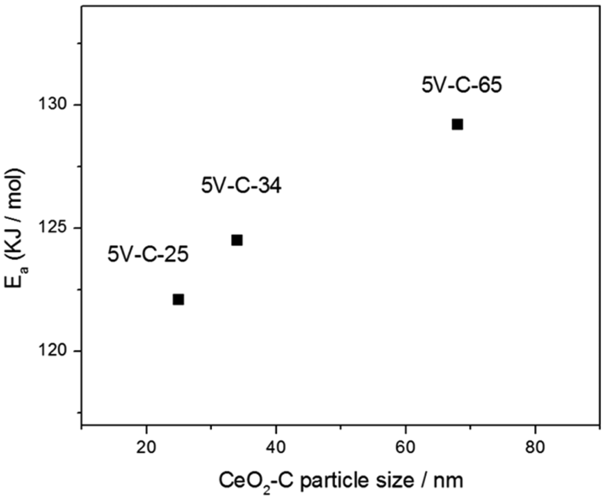

Figure 9. Calculated activation energy (E_a) for HCHO formation from surface CH_3O• intermediates' decomposition on 5 V-CeO_2−C catalysts as a function of support size.

4. DISCUSSION

In this work, CeO_2 nanocubes with different sizes were prepared hydrothermally in the presence of NaOH. Our previous study has demonstrated that Na has some detrimental effects on VO_x/CeO_2 catalysis in methanol ODH. Specifically, when Na/V ratios are higher than 0.25, the presence of Na impurity can change the surface acidity/basicity of VO_x/CeO_2 by titrating the Brønsted acid sites, alter the structure of active sites, suppress the reducibility of VO_x species, and decrease the activity of VO_x/CeO_2 catalysts and selectivity to formaldehyde.[15] The VO_x/CeO_2 catalysts used in this study were thoroughly washed with methanol and deionized water. XPS was performed to ensure the absence of Na in these samples (Figure S3).

It has been reported that oxygen vacancies in CeO_2 are energetically more favored on the surface than in the bulk.[28] Previous research has indicated that the oxygen vacancy density is affected by the exposed facets. For example, DFT calculation shows that oxygen vacancy formation energy on CeO_2 facets follows the trend (110) < (100) < (111).[29,30] In the present study, Raman spectra of the three ceria nanocube samples (Figure 5) demonstrate that for samples with the same dominating facets, the oxygen defect density (the 594 cm^{-1} feature) can further be systematically varied by varying particle sizes. As is shown in Figure 5, smaller ceria nanocubes display higher oxygen vacancy densities, which is in line with the presence of more terrace, step, and corner sites on the surfaces of smaller ceria nanocubes. Oxygen defects can promote redox processes by increasing oxygen mobility.[31] This notion is nicely reflected in the lower reduction temperatures of surface CeO_2 species on smaller ceria nanocubes, as shown by H_2-TPR (Figure 4).

The addition of VO_x species also imposes an effect on the oxygen defect sites. Theoretical calculations show that deposition of VO_x to CeO_2 supports reduces the oxygen defect formation energy on the surface;[26] however, previous UV-Raman study shows that the number of oxygen defect sites decreases continuously with increasing VO_x loading.[24] These collectively suggest that some VO_x deposit precisely on surface oxygen defect sites to eliminate them. It has been reported previously that in VO_x/CeO_2 catalysts, two extra electrons upon oxygen removal are localized in the Ce 4f state, reducing two surface Ce sites to $Ce^{3+}(f^1)$ ions and V is stabilized in a 5+ oxidation state (d^0).[26] Raman results in this study (Figure 7) show that with the addition of VO_x species, the oxygen vacancy density on 5 V/CeO_2 catalysts still follows the same trend as the parent ceria supports; namely, in the order of 5 V-CeO_2-25 > 5 V-CeO_2-34 > 5 V-CeO_2-68.

The VO_x species supported on smaller CeO_2 nanocubes exhibit lower reduction temperatures (Figure 4), demonstrating that the density of oxygen defects on CeO_2 nanocubes affect the redox ability of surface VO_x sites. It is worth noting that the change in the reduction of VO_x species on CeO_2 supports is not likely caused by the degree of polymerization of the VO_x species. From the Raman spectra shown in Figure 6, VO_x dispersion appears to be very similar on the three supports. It is important to note that upon VO_x deposition, the low temperature reduction peaks between ∼350 to 460 °C for surface CeO_2 diminish. This suggests that (1) at least a portion of VO_x species are directly deposited on CeO_2 surface sites that are responsible for H_2 activation or (2) strong electronic interactions between CeO_2 and VO_x species so that redox for CeO_2 is greatly passivated. However, it is not clear which type of oxygen defect, surface or subsurface, plays more important roles in influencing redox properties for the surface VO_x catalytic centers.

As shown by methanol TPD results in Figure 8, the HCHO formation temperature on VO_x/CeO_2 nanocubes increases in the order 5 V−C-68 > 5 V−C-34 > 5 V−C-25, indicating that the activation energy for methoxyl decomposition on VO_x/CeO_2 catalysts follows the order of 5 V−C-25 < 5 V−C-34 < 5 V−C-68. This trend correlates very well with the trend for VO_x reduction in H_2-TPR (Figure 4). Furthermore, the trend is also in good agreement with the oxygen vacancy density in these catalysts: for VO_x catalysts on smaller CeO_2 with higher oxygen vacancy density, lower activation energy for methoxyl decomposition was observed. As shown above, the presence of slightly higher percentages of exposed non-(100) surfaces on smaller ceria nanocubes contributes to higher oxygen vacancy densities. However, since average TOFs in methanol ODH on VO_x catalysts supported on various CeO_2 facets are within the same order of magnitude,[12] these minor sites (<9%) are not expected to provide the majority of activities for samples used in the present study. In other words, the activity trend observed for the three samples here should not change because of the differences in their exposed non-(100) sites. Therefore, it appears rather logical that oxygen vacancies from the supports provide beneficial effects on facilitating the redox process of VO_x species as well as the decomposition of the adsorbed methoxyl groups. The results from the present study further corroborate our previous proposal that the presence of oxygen vacancies on VO_x/CeO_2 catalysts plays important roles in promoting methanol ODH. Theoretical study by Bell and coworker on VO_x/TiO_2 catalysts suggested that introduction of oxygen vacancies adjacent to the VO_x species will reduce the activation energy for the rate-limiting step, H abstraction from methoxy group, by providing an active site with more flexibility and allowing for a larger degree of H-bonding, and therefore promote the activity of VO_x catalysts.[8] In the present study, by minimizing effects from (110) and (111) facets via controlled support synthesis and by varying the oxygen defect density by controlling the support particle size, we further prove that the oxygen defects impose important influences on the activity of supported vanadia catalysts for methanol oxidation.

5. CONCLUSION

Ceria nanocubes with controlled sizes were synthesized and used for the synthesis of high-surface-area model supported VO_x catalysts. The catalytic properties of such prepared VO_x/CeO_2 nanocubes were further investigated in methanol oxidation reaction. Combined TEM, SEM, XRD, and Raman studies reveal that the oxygen defect density of VO_x/CeO_2 catalysts can be tuned by controlling the particle size of ceria nanocubes with dominant (100) facets. H_2-TPR results indicate that the presence of oxygen defects may also facilitate the redox ability of VO_x species. VO_x species supported on smaller nanocubes exhibit a lower activation energy for methoxy decomposition, according to the methanol TPD study. With the minimized effect of minor facets, including (110) and (111) on the structure of VO_x species, the promoted activity of VO_x catalysts on smaller ceria nanocubes can be attributed to the presence of more oxygen vacancies, which effectively lowers the reaction barrier of the rate-limiting step (C−H cleavage in methoxy) in the ODH of methanol, thus promoting the reactivity of supported VO_x catalysts.

■ ASSOCIATED CONTENT

Ⓢ Supporting Information

The following file is available free of charge on the ACS Publications website at DOI: 10.1021/cs502084g.

> Additional characterization data including high resolution TEM images, methanol TPD spectra and XPS spectra are available in Supporting Information (PDF)

■ AUTHOR INFORMATION

Corresponding Authors

*Phone: +1(509)3717164. Fax: +1(509)3716066. E-mail: feng.gao@pnnl.gov.

*Phone: +1(509)3716273. Fax: +1(509)3716242. E-mail: yong.wang@pnnl.gov.

Notes

The authors declare no competing financial interest.

■ ACKNOWLEDGMENTS

We gratefully acknowledge financial support from the U.S. Department of Energy (DOE), Office of Basic Energy Sciences, Division of Chemical Sciences, Geosciences, and Biosciences. Part of this work was conducted in the William R. Wiley Environmental Molecular Sciences Laboratory (EMSL), a national scientific user facility sponsored by DOE's Office of Biological and Environmental Research and located at Pacific Northwest National Laboratory (PNNL). PNNL is a multi-program national laboratory operated for the DOE by Battelle.

■ REFERENCES

(1) Wachs, I. E.; Deo, G.; Weckhuysen, B. M.; Andreini, A.; Vuurman, M. A.; deBoer, M.; Amiridis, M. D. *J. Catal.* **1996**, *161*, 211−221.

(2) GrzybowskaSwierkosz, B.; Trifiro, F. *Appl. Catal., A* **1997**, *157*, 1−2.

(3) Bond, G. C.; Konig, P. *J. Catal.* **1982**, *77*, 309−322.

(4) Zhao, C. L.; Wachs, I. E. *J. Catal.* **2008**, *257*, 181−189.

(5) Wachs, I. E. *Appl. Catal., A* **2011**, *391*, 36−42.

(6) Gao, X. T.; Bare, S. R.; Fierro, J. L. G.; Wachs, I. E. *J. Phys. Chem. B* **1999**, *103*, 618−629.

(7) Burcham, L. J.; Badlani, M.; Wachs, I. E. *J. Catal.* **2001**, *203*, 104−121.

(8) Goodrow, A.; Bell, A. T. *J. Phys. Chem. C* **2008**, *112*, 13204−13214.

(9) Beck, B.; Harth, M.; Hamilton, N. G.; Carrero, C.; Uhlrich, J. J.; Trunschke, A.; Shaikhutdinov, S.; Schubert, H.; Freund, H.-J.; Schlögl, R.; Sauer, J.; Schomäcker, R. *J. Catal.* **2012**, *296*, 120−131.

(10) Carrero, C. A.; Keturakis, C. J.; Orrego, A.; Schomacker, R.; Wachs, I. E. *Dalton Transactions* **2013**, *42*, 12644−12653.

(11) Wachs, I. E. *Catal. Today* **2005**, *100*, 79−94.

(12) Li, Y.; Wei, Z.; Gao, F.; Kovarik, L.; Peden, C. H. F.; Wang, Y. *J. Catal.* **2014**, *315*, 15−24.

(13) Wu, Z. L.; Schwartz, V.; Li, M. J.; Rondinone, A. J.; Overbury, S. H. *J. Phys. Chem. Lett.* **2012**, *3*, 1517−1522.

(14) Mai, H. X.; Sun, L. D.; Zhang, Y. W.; Si, R.; Feng, W.; Zhang, H. P.; Liu, H. C.; Yan, C. H. *J. Phys. Chem. B* **2005**, *109*, 24380−24385.

(15) Li, Y.; Wei, Z. H.; Sun, J. M.; Gao, F.; Peden, C. H. F.; Wang, Y. *J. Phys. Chem. C* **2013**, *117*, 5722−5729.

(16) Abbott, H. L.; Uhl, A.; Baron, M.; Lei, Y.; Meyer, R. J.; Stacchiola, D. J.; Bondarchuk, O.; Shaikhutdinov, S.; Freund, H. J. *J. Catal.* **2010**, *272*, 82−91.

(17) Lin, Y.; Wu, Z.; Wen, J.; Poeppelmeier, K. R.; Marks, L. D. *Nano Lett.* **2013**, *14*, 191−196.

(18) Pan, A. Q.; Zhang, J. G.; Nie, Z. M.; Cao, G. Z.; Arey, B. W.; Li, G. S.; Liang, S. Q.; Liu, J. *J. Mater. Chem.* **2010**, *20*, 9193−9199.

(19) Wu, Z. L.; Li, M. J.; Overbury, S. H. *ChemCatChem* **2012**, *4*, 1653−1661.

(20) Trovarelli, A. *Catal. Rev.: Sci. Eng.* **1996**, *38*, 439−520.

(21) Taniguchi, T.; Watanabe, T.; Sugiyama, N.; Subramani, A. K.; Wagata, H.; Matsushita, N.; Yoshimura, M. *J. Phys. Chem. C* **2009**, *113*, 19789−19793.

(22) Wu, Z. L.; Li, M. J.; Howe, J.; Meyer, H. M.; Overbury, S. H. *Langmuir* **2010**, *26*, 16595−16606.

(23) Baron, M.; Abbott, H.; Bondarchuk, O.; Stacchiola, D.; Uhl, A.; Shaikhutdinov, S.; Freund, H.-J.; Popa, C.; Ganduglia-Pirovano, M. V.; Sauer. *Angew. Chem., Int. Ed.* **2009**, *48*, 8006−8009.

(24) Wu, Z. L.; Rondinone, A. J.; Ivanov, I. N.; Overbury, S. H. *J. Phys. Chem. C* **2011**, *115*, 25368−25378.

(25) Feng, T.; Vohs, J. M. *J. Catal.* **2002**, *208*, 301−309.

(26) Ganduglia-Pirovano, M. V.; Popa, C.; Sauer, J.; Abbott, H.; Uhl, A.; Baron, M.; Stacchiola, D.; Bondarchuk, O.; Shaikhutdinov, S.; Freund, H. J. *J. Am. Chem. Soc.* **2010**, *132*, 2345−2349.

(27) Kim, T.; Wachs, I. E. *J. Catal.* **2008**, *255*, 197−205.

(28) Nolan, M.; Fearon, J. E.; Watson, G. W. *Solid State Ionics* **2006**, *177*, 3069−3074.

(29) Nolan, M.; Parker, S. C.; Watson, G. W. *Surf. Sci.* **2005**, *595*, 223−232.

(30) Yang, Z. X.; Woo, T. K.; Baudin, M.; Hermansson, K. *J. Chem. Phys.* **2004**, *120*, 7741−7749.

(31) Paier, J.; Penschke, C.; Sauer, J. *Chem. Rev.* **2013**, *113*, 3949−3985.